

*Full Length Research Paper*

# Three-dimensional coastal water front reconstruction from RADARSAT-1 synthetic aperture radar (SAR) satellite data

**Maged Marghany**

Institute of Geospatial Science and Technology (INTEG), Universiti Teknologi Malaysia, 81310 UTM, Skudai, Johore Bahru, Malaysia. E-mail: [maged@utm.my](mailto:maged@utm.my) or [magedupm@hotmail.com](mailto:magedupm@hotmail.com).

Accepted 18 October, 2011

**This paper presents work done to utilize RADARSAT-1 synthetic aperture radar (SAR) data to reconstruct 3-D of coastal water front. The velocity bunching model was used to extract the significant wave height from RADARSAT-1 SAR, while the Volterra model was used to model the front movements. B-spline also was implemented to reconstruct the front into 3-D. This study shows that the integration between velocity bunching, Volterra models and B-spline can be used as geomatica tool for 3-D front reconstruction.**

**Key words:** RADARSAT-1 SAR, Volterra model, front, velocity bunching, 3-D.

## INTRODUCTION

An ocean front is a boundary separating two masses into water of different densities, and is the primary cause of gradient change of physical ocean properties. The water masses that are separated by a front, usually differ in temperature and salinity. Fronts occur on a wide range of scales, starting with those formed within an estuary between inflowing water and the estuary water. Other fronts are found on the continental shelf, separating a zone from coastal water from oceanic water or stratified water mass from one which is vertically mixed. Fronts also occur on a large-scale in the deep ocean, between water masses of different properties. The boundary between warm, salty subtropical waters and Antarctic waters was found in all three ocean basins. A commonly used criterion is that it is found at the latitude at which the salinity at a depth of 100 m drops below 34.9 practical salinity units. The essential feature of a front bordering a plume is the density difference between water on the two sides of it but other features are often present, enabling it to be detected visually. There is often a colour difference between water masses, arising from a greater concentration of phytoplankton or suspended particles in one than the other. The front itself is frequently marked by a line of foam or floating debris. Bowman and Iverson (1978) stated that the foam line is located at the surface convergence, the detritus line where buoyant objects are trapped by currents moving in opposite directions at the

surface and near the interface and the colour front where upwelled light undergoes a distinct spectral shift approximately the steeply descending isopycnals (Bowden, 1983).

Dynamically, fronts are of considerable importance to understand turbulent energy cascade from ocean surface down to billow-turbulence scales of a few meters (Robinson, 1995). Coastal pollutant material transports are directed by turbulent energy flow vertically through water body. As well, productivity of ocean can would have been enhanced due to fronts since they tend to bring nutrient rich water. Scientists reported that fish stocks increased as a result of the combination of warm water and nutrients arising from cross-frontal mixing. Additionally, fronts also have a great deal to insure search and rescue operations, since a drifting stricken small craft will remain in a front, even when exposed to considerable wind, particularly when it is partly filled with water and nearly completely submerged (Simpson and Pingree, 1978; Bowden, 1983; Robinson, 1995). Although, conventional methods for front studies depend on *in-situ* measurements of sea water temperature and salinity, but they might be costly and time consuming. Isothermal, isohaline contours and water mass diagrams are established procedures for front detection, nevertheless front cannot be visualised in large scale surface ocean (Simpson, 1981; Bowden, 1983).

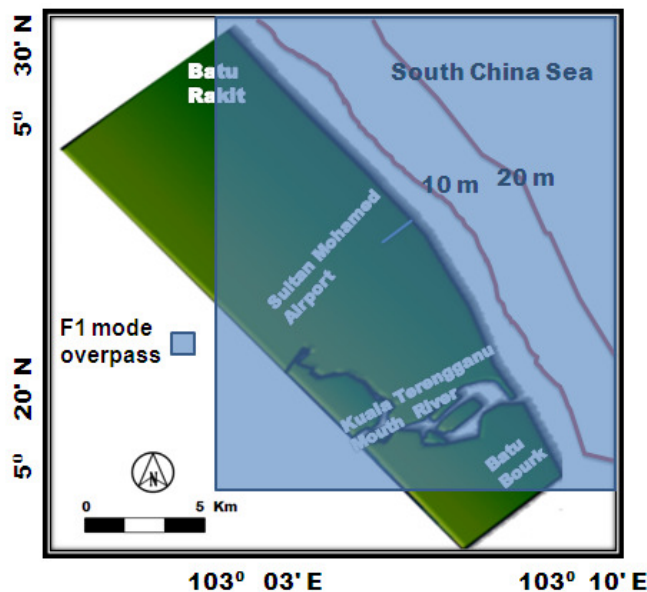


**Figure 1.** RADARSAT-1 SAR F1 mode data passover study area.

According to aforementioned, remote sensing techniques are able to image front locations in large-scale ocean. Both thermal and microwave remote sensing techniques are good tools to identify front locations. For instance, satellite infrared imagery can image front locations because of their strong thermal signatures. Likewise, satellite visible bands are also cable to image fronts based on imaging different colors of the two water masses. Besides that, synthetic aperture radar (SAR) is also able to identify front as a result of abrupt changes of surface wave pattern across front led to exceeding change cross backscatter of SAR data. In this regard, Johannessen et al. (1996) stated that SAR images can sometimes be used to interpret frontal dynamics, including growth and decay of meanders. Recently, Jiang et al. (2009) exploited various remote sensing data. Satellite images obtained from the advanced very HIGH resolution radiometer (AVHRR), the moderate resolution imaging spectroradiometer (MODIS), the sea-viewing wide field-of-view sensor (SeaWiFS) and RADARSAT-1 SAR S1 mode data to study coastal water plume and front which was also captured in S1 mode data.

Consistent with Klemas (2011) remote sensors utilize their dissimilarities in turbidity, color, temperature or salinity from surrounding water environments, to detect and map fronts and plumes. Various remote sensors exploited to study fronts, which involve multispectral and hyperspectral imagers, thermal infrared (TIR) radiometers, microwave radiometers and synthetic aperture radar (SAR). Mounted on satellites and aircraft, these sensors provide the spatial/temporal resolution and coverage needed for tracking plumes and fronts, including their

high temporal and spatial variability.

Scientists have used conventional methodical algorithms to comprehend the complexity of various system interactions. In this regard, imaging coastal feature in synthetic aperture radar (SAR) requires standard mathematical algorithms have been reported recently (Zaki, 2007; Messaoudi et al., 2007; Stephen, 2009; Adeyemo and Fred, 2009; Mehmet, 2009; Ugwu, 2009; Akintorinwa and Adesoji, 2009; Boumaza et al., 2009; Anjamrooz, 2011; Anjamrooz et al., 2011; Khadijeh et al., 2011; Guillermo et al., 2011; Murat, 2011; Mustafa, 2011).

In this paper, we address how 3-D front can be reconstructed from single SAR data (namely the RADARSAT-1 SAR) using integration of Volterra kernel (Inglad and Garello, 1990), velocity bunching and Fuzzy B-spline models (Marghany et al., 2010 and Marghany and Mazlan 2010). There are about three hypothesis that examined are: (i) the use of Volterra model to detect front flow pattern in RADARSAT-1 SAR  $C_{HH}$  band; (ii) the use of velocity bunching model to acquire significant wave height from RADARSAT-1 SAR data; and (iii) to utilize fuzzy B-spline to remodel 3-D of front surface.

## METHODOLOGY

### Study area

The study area is situated in the South China Sea between 5°21' N to 5°25' N, East Coast of Peninsular Malaysia (Figure 1). Consistent with Marghany et al. (2009), there are four seasons: the two monsoons and the two transitional inter-monsoon periods. The monsoon winds and tidal effects (Marghany et al., 2010) affect the seas around Malaysia. The winds during the northeast monsoon are normally stronger than the southwest monsoon (Marghany, 2004). The accompanying waves are with a height that exceeds 3 m (Marghany, 1994). The bathymetry near the area has gentle slopes with 40 m water depth (Figure 1). A clear feature of this area is the primary hydrologic communications between the estuary and the South China Sea. As stated by Marghany et al. (2010) this estuary is the largest estuary along the Terengganu coastline.

### Data set and *in-situ* measurement

The RADARSAT-1 SAR fine mode data were acquired on March 26, 2004, over the coastline of Kuala Terengganu, Malaysia (103° 5' E to 103° 9'E and 5° 20' N to 5° 27' N) (Figure 1). The RADARSAT-1 SAR fine mode data acquire information using C band HH polarized of frequency 5.3 GHz. The swath width of RADARSAT-1 SAR fine mode sensor is 50 km, with the range resolution of 8 to 9 km. There are two numbers of looks for the RADARSAT-1 SAR and the incident angle of 35° to 49° (RADARSAT, 2010).

Ocean wave spectra parameters, such as wavelength, direction and significant wave height are collected using acoustic wave and current (AWAC) wave rider buoy during satellite pass over. AWAC wave rider buoy is deployed 6 h before and satellite passover.

### 3-D front model

There are three algorithms involved for 3-D front reconstruction;

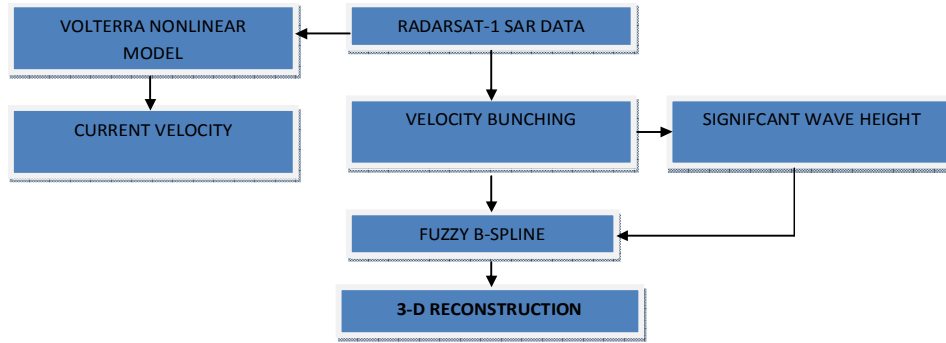


Figure 2. Block diagram for RADARSAT-1 SAR data processing.

velocity bunching, Volterra and fuzzy B-spline. Significant wave heights are simulated from RADARSAT-1 SAR image by using velocity bunching model. Fuzzy B-spline used significant wave height information to reconstruct 3-D front. Moreover, front flow pattern is modeled by Volterra model (Figure 2).

**Velocity bunching model**

In this study, two dimensional Fourier transform (2-DFFT) has been applied to a single SAR image frame consisting of 512 × 512 image pixels which were extracted from RADARSAT-1 SAR image. The Gaussian algorithm was applied to remove the noise from the image and smoothen the wave spectra into normal distribution curve. The band used in this processing is C<sub>HH</sub>-band. Each pixel represents a 12.5 × 12.5 m area for RADARSAT-1 SAR image. The entire image frame of RADARSAT-1 SAR image corresponds to a 6.4 × 6.4 km patches on the ocean surface. This frame size provides a sufficient large area to include at least 10 cycles of very long surface waves, up to 640 m in length, which can be included in a single image frame. It is also small enough to show that the ocean can be reasonably assumed homogeneous within a frame (Marghany, 2004; Marghany and Mazlan, 2010).

The velocity bunching modulation transfer function (MTF) is the dominant component of the linear MTF for the ocean waves with an azimuth wave number ( $k_x$ ). According to Alpers et al. (1981) and Vachon et al. (1993, 1994, 1995, 1997), the velocity bunching can contribute to linear MTF based on the following equation:

$$M_v = \frac{R}{V} \omega \left[ \frac{k_x}{k} \sin \theta + i \cos \theta \right] \tag{1}$$

where  $R/V$  is the scene range to platform velocity ratio, which is 111 s in the case of RADARSAT-1 SAR image data,  $\theta$  is RADARSAT-1 SAR image incidence angel (35 to 49°) and  $\omega$  is the wave spectra frequency which equals to  $2\pi/K$ . To estimate the velocity bunching spectra  $S_{vb}(k)$ , we modified the algorithm that was introduced by Krogstad and Schyberg (1991). The modification is to multiply the velocity bunching MTF ( $M_v$ ) by RADARSAT-1 SAR image spectra variance of the azimuth shifts. This can be calculated by using the following formula:

$$S_{vb}(k) = [I_0 \sum_{n=1}^{\infty} \frac{\psi(k_x)^{2n}}{n!} S_{\zeta\zeta}^{*n} \psi(k)^2 e^{-K_x^2 \rho_{\zeta\zeta}}] [M_v] \tag{2}$$

where  $S_{\zeta\zeta}$  is the SAR spectra variance of the azimuth shifts due to the surface motion, which was induced by the velocity bunching effect in azimuth direction due to high value of  $R/V$ . Furthermore, SAR spectra of ocean wave images have a characteristic of azimuth cutoff and also have an intrinsic azimuth cutoff that in many cases fit very well with actual observation and relates to the cutoff directly to the standard deviation of the azimuth shift, which may be

compactly related to fundamental sea state parameters.  $\rho_{\zeta\zeta}$  is the variance of the derivative of displacements along the azimuth direction,  $I_0$  is SAR image intensity and “\*n” means (n-1)-fold convolution according to Krogsted and Schyberg (1991). Equation 2 was used to draw the velocity bunching spectra energy contours.

Estimation of significant wave height from velocity bunching spectra based on the azimuth cut-off arising from the velocity-bunching model (Equation 2) of the azimuth cutoff could be scaled by the standard deviation of the azimuth shift. Vachon et al. (1993) introduced a relationship between the variance of the derivate of displacement along the azimuth direction  $\rho_{\zeta\zeta}$  and the standard

deviation of the azimuth shift  $\sigma$  which were estimated from the velocity bunching spectra. This relationship was given as (Vachon et al., 1993):

$$\sigma = \sqrt{\rho_{\zeta\zeta}} \tag{3}$$

The relation between standard deviation of the azimuth shift  $\sigma$  and significant wave height  $H_s$  can be given as (Vachon et al., 1994):

$$\sigma = \left(\frac{R}{V}\right) \left(1 - \frac{\sin^2(\theta)}{2}\right)^{0.5} \left(\frac{k_x g}{8}\right)^{0.5} H_s \tag{4}$$

where  $k_x$  is the azimuth wave number,  $\theta$  is RADARSAT-1 SAR image incident angle,  $R/V$  is the scene range to platform velocity ratio and  $g$  is the acceleration due to the gravity. Note that the mean wave period  $T_0$  is equal to  $2\pi(\langle\langle k_x \rangle\rangle g)^{-0.5}$ . Using Equations 6 and 4, the significant wave height  $H_s$  can be obtained:

$$H_s = 0.6(\rho_{\zeta\zeta})^{0.5} \left[ \frac{1 + \theta^2 / 4}{R/V} \right] T_0 \quad (5)$$

where  $\theta$  is the RADARSAT-1 SAR incidence angle and Equation 5 was used to estimate the significant wave height which was based on the standard deviation of the azimuth shift  $\sigma$ .

**Volterra model**

In reference to Inglad and Garelo (1999), Volterra series can be used to model nonlinear imaging mechanisms of surface current gradients by RADARSAT-1 SAR image. As a result of the fact that Volterra linear kernel contained most of the RADARSAT-1 SAR energy which is use to simulate current flow along range direction. Following Inglad and Garelo (1999), Volterra kernel filter has the following expression:

$$H_{1y}(v_x, v_y) = k_y \vec{U} \cdot \frac{\partial x}{\partial u_x} \left[ \vec{K}^{-1} \left[ \frac{\partial}{\partial t} + \frac{\partial \vec{c}_g}{\partial x} + \frac{\partial \vec{u}_x}{\partial x} + 0.043 \frac{(\vec{u}_a \vec{K})^2}{\omega_0} \right] \right] \left[ \frac{\partial \psi}{\partial \omega} \right] \quad (6)$$

$$\frac{\vec{c}_g(\vec{K}) \vec{U} + j 0.043 (\vec{u}_a \vec{K})^2 \omega_0^{-1}}{[\vec{c}_g(\vec{K}) \vec{U}]^2 + [0.043 (\vec{u}_a \vec{K})^2 \omega_0^{-1}]^2} + j (0.6 \cdot 10^{-2} \cdot \vec{K}^{-4}) \left( \frac{R}{V} \right) \vec{u}_x$$

where  $\vec{U}$  is the mean current velocity,  $\vec{u}_x$  is the current flow, while  $\vec{u}_a$  is the current gradient along azimuth direction, respectively.  $k_y$  is the wave number along range direction,  $\vec{K}$  is the spectra wave number,  $\omega_0$  is the angular wave frequency,  $\vec{c}_g$  is the wave velocity group,  $\psi$  is the wave spectra energy and  $R/V$  is the range to platform velocity ratio.

In reference to Inglad and Garelo (1999), the inverse filter  $G(v_x, v_y)$  is use since  $H_{1y}(v_x, v_y)$  has a zero for  $(v_x, v_y)$  which indicates that the mean current velocity should have a constant offset (Majid and Gondal, 2011). The inverse filter  $G(v_x, v_y)$  can be given as:

$$G(v_x, v_y) = \begin{cases} [H_{1y}(v_x, v_y)]^{-1} & \text{if } (v_x, v_y) \neq 0, \\ 0 & \text{otherwise.} \end{cases} \quad (7)$$

Using Equation 6 into 7, range current velocity  $U_y(0, y)$  can be estimated by:

$$U_y(0, y) = I_{RADARSAT-ISAR} \cdot G(v_x, v_y) \quad (8)$$

where  $I_{RADARSAT-ISAR}$  is the frequency domain of Radarsat-1 SAR image acquired by applying 2-D Fourier transform on RADARSAT-1 SAR image.

**The fuzzy B-splines method**

Fuzzy B-spline concept adopted from Anile et al. (1995) and Anile (1997) which shows excellent 3-D reconstruction stated by Marghany et al. (2010) and Marghany and Mazlan (2011).

Considering significant wave height modeled by using velocity bunching and radar backscatter cross section across front, fuzzy numbers are created. In doing so, two basic notions of confidence interval and presumption level were considered (Hassasi and Saneifard, 2011). A confidence interval is a real values interval which provides the sharpest enclosing range for significant wave height values. An assumption level,  $\mu$ -level is an estimated truth value in the [0, 1] interval of significant wave height changes (Anile, 1997). The 0 value suits to minimum knowledge of significant wave heights and 1 to the maximum of significant wave height. A fuzzy number is then prearranged in the confidence interval set, each one related to an assumption level  $\mu$  [0, 1]. Additionally, the following must hold for each pair of confidence interval which define a number,  $\mu > \mu' \Rightarrow h > h'$ . Let us consider a function  $f : h \rightarrow h$ , of N fuzzy variables  $h_1, h_2, \dots, h_n$ , where  $h_n$  is the global minimum and maximum values of significant wave heights. The construction begins with the same preprocessing to compress the measured significant wave height values into a uniformly spaced grid of cells. Then, a membership function is defined for each pixel which incorporates the degrees of certainty of radar cross backscatter.

**RESULTS AND DISCUSSION**

Figure 3 shows the F1 mode data which was acquired along the coastal water of Kuala Terengganu, Malaysia on the 26 of March, 2004. Figure 3 shows the signature of current boundary which can turn up as a result of brightness frontal curved line. Furthermore, it is clear that the front occurred close to estuary, which is a clear indication of tidal front events. In fact, the interaction of flood tidal current flow from estuary with topography can form a tidal front (Bowden, 1983).

The RADARSAT-1 backscatter cross-section across front has a maximum value of -21.25 dB. The maximum backscatter value of 0.33 dB is found across the brightness frontal line. Moreover, the variation of radar backscatter cross-section is due to the current boundary gradient. According to Vogelzang et al. (1997), ocean current boundaries are often accompanied by the changes in the surface roughness that can be detected by SAR. These surface roughness changes are due to the interaction of surface waves directly with surface current gradients. These interactions can cause an increase in the surface roughness and radar backscatter (Shuchman and LyzengaL, 1985).

Figure 4 shows 3-D front reconstruction with significant wave heights and current variations cross front. Figure 4 shows that significant wave variation cross front with maximum significant wave height of 1.2 m and gradient current of 0.9 m/s. March represents the northeast monsoon period as coastal water currents in the South China Sea tend to move from the north direction (Marghany et al., 2010). Nevertheless, Figure 4 shows a meander current with southward direction. In fact, this current is created because of the water inflow from Kuala Terengganu Mouth River. Furthermore, Marghany (1994) and Marghany and Mazlan (2010) quoted that strong tidal

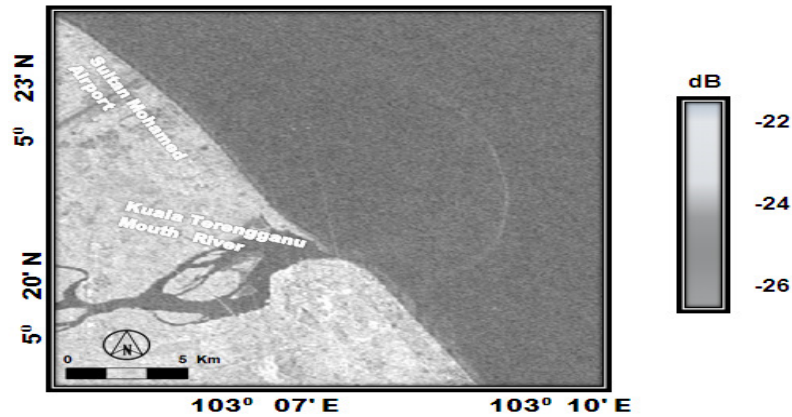


Figure 3. Backscatter variations in F1 mode data.

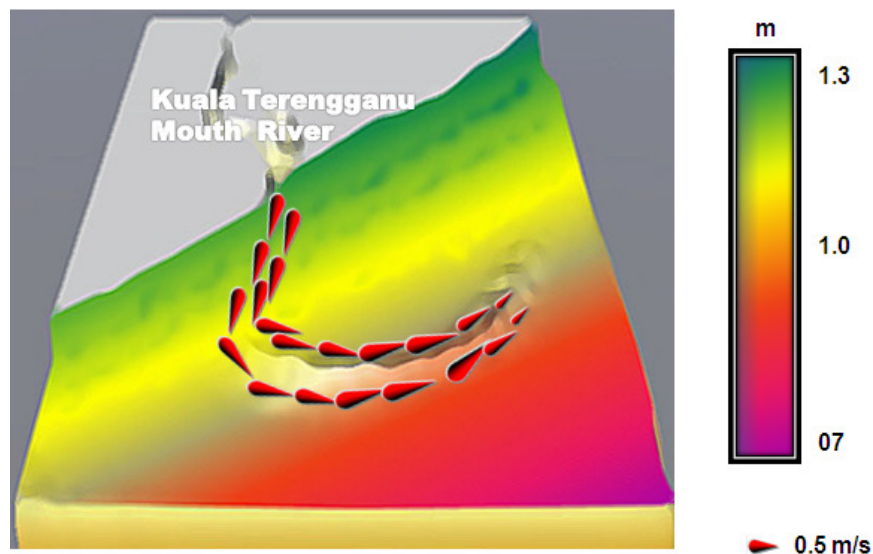


Figure 4. 3-D front reconstruction with significant wave height ( $H_s$ ) and surface current variations ( $U_y$ ).

current is a dominant feature in the South China Sea with maximum velocity of 1.5 m/s. Clearly, 3-D front coincides with water depth between 10 and 20 m (Figure 5). This indicates shallow water, where the strong tidal stream (Figure 4) causes vertical mixing. Marghany (1994) found that the thermocline and halocline layers occurred in water depth of 20 m. This means that the front occurred between well mixed and stratified water column.

The visualization of 3-D front is sharp with the RADARSAT-1 SAR  $C_{HH}$  band, because each operation on a fuzzy number becomes a sequence of corresponding operations on the respective  $\mu$  and  $\mu'$  levels, and the multiple occurrences of the same fuzzy parameters were evaluated as a result of the function on fuzzy variables (Anile, 1997). Typically, in computer graphics, two objective quality definitions for fuzzy B-

splines were used: triangle-based criteria and edge-based criteria. Triangle-based criteria follow the rule of maximization or minimization, respectively, the angles of each triangle. The so-called max-min angle criterion prefers short triangles with obtuse angles. In addition, the fuzzy B-spline depicts optimize locally triangulation between two different points (Anile et al., 1995). This corresponds to the feature of deterministic strategies of finding only sub-optimal solutions which usually overcomes uncertainties. In this context, the spatial cluster of gradient flow at each triangulation points can be simulated (Figure 4). Consequently, triangle-based criteria follow the rule of maximization or minimization, respectively, of the angles of each triangle (Fuchs et al., 1997) which prefers short triangles with obtuse angles. Furthermore, edge-based criteria prefer edges that are closely related. This study confirms the previous studies

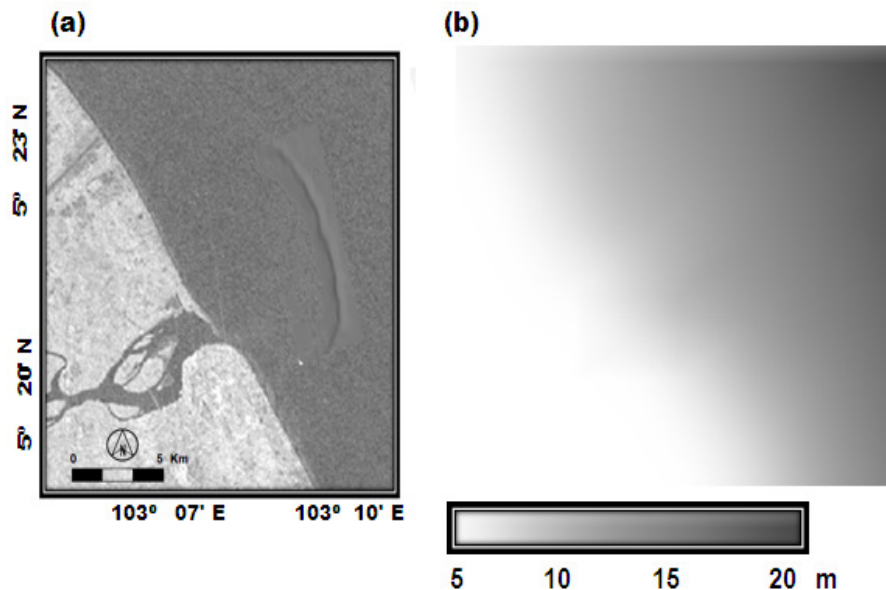


Figure 5. F1 mode data for (a) 3-D front and (b) coastal bathymetry.

of Anile et al. (1995), Fuchs et al. (1997) and Marghany et al. (2010). Indeed, these studies have agreed that fuzzy B-spline algorithm is an accurate tool for 3-D surface reconstruction from 2-D data (Marghany and Mazlan, 2011).

## Conclusion

This work has demonstrated procedure to reconstruct 3-D coastal front in RADARSAT-1 SAR F1 mode data. Three algorithms of velocity bunching, Volterra and fuzzy B-spline are used to reconstruct 3-D coastal front. The velocity bunching algorithm modeled significant wave height, Volterra algorithm simulated coastal current movement while fuzzy B-spline implemented the significant wave height to reconstruct 3-D coastal front. The study shows that the significant wave height varied between 0.7 and 1.3 m across the front. The front is dominated by strong tidal current that ranged between 0.9 and 1.5 m/s. This front occurred in water depth of 20 m. Additionally, fuzzy B-spline reconstructed 3-D front with smooth graphic feature. Indeed, fuzzy B-spline tracked the smooth and rough surface. Finally, fuzzy B-spline algorithm can keep track of uncertainty together with representing spatially clustered gradient of flow points across the front. In conclusion, fuzzy B-spline algorithm can be used for 3-D front reconstruction with integration of velocity bunching and Volterra algorithm.

## REFERENCES

Adeyemo J, Fred O (2009). Optimizing planting areas using differential evolution (DE) and linear programming (LP). *Int. J. Phys. Sci.*, 4(4): 212-220.

Alpers WR, Ross DB, Rufenach CL (1981). On the detectability of ocean surface waves by real and synthetic aperture radar. *J. Geophys. Res.*, 86: 6481-6498.

Anile AM (1997). *Report on the activity of the fuzzy soft computing group*, Technical Report of the Dept. of Mathematics, University of Catania, March 1997, p. 10.

Anile AM, Deodato S, Privitera G (1995) *Implementing fuzzy arithmetic*, Fuzzy Sets and Systems, p. 72.

Anjamrooz SH (2011). Trinity is a numerical model of the holographic universe. *Int. J. Phys. Sci.*, 6(2): 175-181.

Anjamrooz SH, McConnell DJ, Azari H (2011). The cellular universe: A new cosmological model based on the holographic principle. *Int. J. Phys. Sci.*, 6(9): 2175-2183.

Boumazza N, Benouaz T, Chikhaoui A, Cheknane A (2009). Numerical simulation of nonlinear pulses propagation in a nonlinear optical directional coupler. *Int. J. Phys. Sci.*, 4(9): 505-513.

Bowden KF (1983). *Physical oceanography of coastal waters*. Ellis Horwood Ltd. England. 302p.

Guillermo D, Genaro LT, Soto-Zarazúa Ramón M, Guevara-González Enrique Rico-García G (2011). Bayesian networks for defining relationships among climate factors. *Int. J. Phys. Sci.*, 6(18): 4412-4418.

Inglad J, Garello R (1999). Depth estimation and 3D topography reconstruction from SAR images showing underwater bottom topography signatures. In *Proceedings of IGARSS'99*.

Jiang L, Yang XH, Klemas V (2009). Remote sensing for the identification of coastal plumes: case studies of Delaware Bay. *Int. J. Remote Sensing*, 30(8): 2033-2048.

Johannessen JARA, Shuchma G, Digranes DR, Lyzenga, C, Wackerman O, Johannessen M, Vachon PW (1996). Coastal Ocean fronts and eddies imaged with ERS 1 synthetic aperture radar. *J. Geophys. Res.*, 101(C3): 6651-6667

Hassasi N, Saneifard R (2011). A novel algorithm for solving fuzzy differential inclusions based on reachable set. *Int. J. Phys. Sci.*, 6(9): 4712-4716.

Khadijeh M, Motameni H, Enayatifar R (2011). New method for edge detection and de noising via fuzzy cellular automata. *Int. J. Phys. Sci.*, 6(13): 3175-3180.

Klemas V (2011) *Remote Sensing of Coastal Plumes and Ocean Fronts: Overview and Case Study*. J. Coastal Res. In-Press.

Krogstad HE, Schyberg H (1991). On Hasselman's nonlinear ocean – SAR transformation, *Proc. of IGARSS'91*, held at Espo, Finland from Jun. 3-6, pp. 841-849.

- Fuchs H, Kedem ZM, Ussellon SP (1997). Optimal Surface Reconstruction from Planar Contours. *Commun. ACM.*, 20: 693-702.
- Majid K, Gondal MA (2011). An efficient two step Laplace decomposition algorithm for singular Volterra integral equations. *Int. J. Phys. Sci.*, 6(20): 4717-4720.
- Marghany M (1994). Coastal Water Circulation off Kuala Terengganu, Malaysia". MSc. Thesis Universiti Pertanian Malaysia. <http://psasir.upm.edu.my/12308/>
- Marghany M (2004). velocity Bunching Model for Modelling wave Spectra Along east Coast of Malaysia. *J. Indian Society Remote Sensing.*, 32(2): 185-198.
- Marghany M, Mazlan H, Cracknell AP (2010). 3-D visualizations of coastal bathymetry by utilization of airborne TOPSAR polarized data. *Int. J. Dig. Ear.*, 3(2): 187-206.
- Marghany M, Mazlan H (2010). Simulation of sea surface current velocity from synthetic aperture radar (SAR) data. *Int. J. Phys. Sci.*, 5(12): 1915-1925.
- Marghany M, Mazlan H (2011). Optical digital sensor for three-dimensional turbulent flow visualization. *Int. J. Phys. Sci.*, 6(3): 506-510.
- Mehmet K (2009). An analytical expression for arbitrary derivatives of Gaussian functions  $\exp(ax^2)$ . *Int. J. Phys. Sci.*, 4(4): 247-249.
- Messaoudi M, Sbita L, Abdelkrim MN (2007). A robust nonlinear observer for states and parameters estimation and on-line adaptation of rotor time constant in sensor less induction motor drives. *Int. J. Phys. Sci.*, 2(8): 217-225.
- Murat KK (2011). Weakened Mannheim curves. *Int. J. Phys. Sci.*, 6(20): 4700-4705.
- Mustafa B (2011). Natural lift curves and the geodesic sprays for the spherical indicatrices of the involutes of a time like curve in Minkowski 3-space. *Int. the Phys. Sci.*, 6(20): 4706-4711.
- Robinson IS (1995). *Satellite Oceanography: An Introduction for Oceanographers and Remote –sensing Scientists.* Johan Wiley & Sons. New York. 455p.
- Shuchman RA, Lyzenga DR, Meadows GA (1985). Synthetic aperture radar imaging of ocean-bottom topography via tidal-current interactions: theory and observations, *Int. J. Rem. Sens.*, 6: 1179-1200.
- Simpson JH (1981). The shelf-sea fronts: implications of their existence and behaviour. *Philosophical Transactions of the Royal Society of London A302*: 531-546.
- Simpson JH, Pingree RD (1978). Shallow sea fronts produced by tidal stirring. In: M. J. Bowman and W. E. Esaias (editors): *Oceanic fronts in coastal processes.* Springer, Berlin, pp. 29-42.
- Stephen EU (2009). Modified-accelerated Krawczyk's algorithm. *Int. J. Phys. Sci.*, 4(2): 047-052.
- Vachon PW, Raney RK, Krogstad HE, Liu AK (1993). Airborne synthetic aperture radar observations and simulations for waves-in-Ice. *J. Geophys. Res.*, 98(16): 411-16,425.
- Vachon PW, Krogstad HE, Paterson JS (1994). Airborne and spaceborne synthetic aperture radar observations of ocean waves. *Atmosphere-Ocean.* 32(10): 83-112.
- Vachon PW, Liu AK, Jackson FC (1995). Near-shore wave evolution observed by airborne SAR during SWADE. *Atmosphere-Ocean*, 2: 363-381.
- Vachon PW, Campbell JWM, Dobson FW (1997). Comparison of ERS and RADARSAT SARS for wind and wave measurement. Paper Presented at third ERS Symp., ESA, held at Florence, Italy from Mar. 18-2.
- Vogelzang J, Wensink GJ, Calkoen CJ, van der Kooij MWA (1997). Mapping submarine sand waves with multiband imaging radar, 2, Experimental results and model comparison, *J. Geophys. Res.*, 102: 1183-1192.
- Ugwu E (2009). Analytical study of electromagnetic wave scattering behaviour using Lippmann-Schwinger equation. *Int. J. Phys. Sci.*, 4 (5): 310-312.
- Zaki MS (2007). On asymptotic behaviour of a second order delay differential equation. *Int. J. Phys. Sci.*, 2(7): 185-187.